Received Date : 20-Feb-2018

Revised Date : 14-May-2018

Accepted Date : 21-May-2018

Article type : Regular Paper

Color : Figs 1,3 & 6-9

Polymorphism in disease-related apolipoprotein C-II amyloid fibrils: A structural model for rod-like fibrils

Courtney O. Zlatic[1§], Yu Mao[1§], Nevena Todorova[2§], Yee-Foong Mok[1], Geoffrey J. Howlett[1], Irene Yarovsky[2], Paul R. Gooley[1] and Michael D.W. Griffin[1*]

[1]Department of Biochemistry and Molecular Biology, University of Melbourne, Parkville, Victoria 3010, Australia and Bio21 Molecular Science and Biotechnology Institute, University of Melbourne, Parkville, Victoria 3010, Australia.

[2]School of Engineering, RMIT University, GPO Box 2476V, Melbourne, Victoria 3001, Australia

[§] These authors contributed equally to the work

*To whom correspondence should be addressed: Department of Biochemistry and Molecular Biology, Bio21 Molecular Science and Biotechnology Institute, University of Melbourne, 30 Flemington Road, Parkville, Victoria 3010, Australia. Tel.: 61-3-9035-4233; Fax: 61-3-9348-1421; e-mail: mgriffin@unimelb.edu.au

Running title: Rod-like apoC-II amyloid fibrils

Abbreviations: apo, apolipoprotein; GuHCl, guanidine hydrochloride; H/D, hydrogen/deuterium; KDDK, K30D-D69K; LysoMPC, 1-Myristoyl-2-Hydroxy-*sn*-Glycero-3-Phosphocholine; MD, molecular dynamics; ThT, thioflavin T; WT, wild-type

Abstract:

Human apolipoprotein (apo) C-II is one of several plasma apolipoproteins that form amyloid deposits *in vivo* and is an independent risk factor for cardiovascular disease. Lipid-free apoC-II readily self-assembles into twisted-ribbon amyloid fibrils but forms straight, rod-like amyloid fibrils in the presence of low concentrations of micellar phospholipids. Charge mutations exerted significantly different effects on rod-like fibril formation compared to their effects on twisted-ribbon fibril formation. For instance, the double mutant K30D, D69K apoC-II readily formed twisted-ribbon fibrils, while the rate of rod-like fibril formation in the presence of micellar phospholipid was negligible. Structural analysis of rod-like apoC-II fibrils using hydrogen/deuterium exchange and NMR analysis showed exchange protection consistent with a core cross-β structure comprising the C-terminal 58-76 region. Molecular dynamic simulations of fibril arrangements for this region favored a parallel cross-β structure. X-ray fibre diffraction data for aligned rod-like fibrils showed a major meridional spacing at 4.6 Å and equatorial spacings at 9.7 Å, 23.8 Å and 46.6 Å. The latter two equatorial spacings are not observed for aligned twisted-ribbon fibrils and are predicted for a model involving two cross-β fibrils in an off-set antiparallel structure with 4 apoC-II units per rise of the β-sheet. This model is consistent with the mutational effects on rod-like apoC-II fibril formation. The lipid-dependent polymorphisms exhibited by apoC-II fibrils could determine the properties of apoC-II in renal amyloid deposits and their potential role in the development of cardiovascular disease.

Keywords: amyloid disease, amyloid fibrils, cardiovascular disease, protein misfolding, mutation, molecular dynamics, apolipoprotein C-II, cross beta structure, polymorphism, ion pair, charge pair, metamorphic protein

Introduction

Mature apolipoprotein (apo) C-II is comprised of 79 amino acids and is a component of very low-density lipoproteins [1]. Plasma levels of apoC-II show a significant association with the incidence of cardiovascular disease, stroke and myocardial infarction [2]. While the mechanism for this association is not known, several observations suggest amyloid fibril formation may be involved. The capacity of apoC-II to form amyloid fibrils *in vivo* is highlighted by recent studies that establish apoC-II as the main protein component in two new types of renal amyloidosis [3, 4]. Members of the apolipoprotein family, including apoA-I, apoA-II, apoA-IV, apoC-II, apoC-III, apoE, serum amyloid A and α-synuclein, are widely associated with amyloid diseases and account for a significant proportion of the list of approximately 36 proteins known to form amyloid fibrils *in vivo*[5, 6]. The limited stability of apolipoproteins in the lipid-free state has been proposed as the structural basis of the wide-spread occurrence of apolipoproteins in amyloid disease [7].

Several apolipoproteins, including apoC-II, deposit in atherosclerotic lesions co-localized with the amyloid marker, serum amyloid P [8]. Amyloid fibrils formed from lipid-free apoC-II induce several markers of the macrophage inflammatory response suggesting an active role for apoC-II in the progression of atherosclerosis [9]. For instance, several receptors implicated in atherogenesis mediate the clearance of amyloid fibrils, including apoC-II and Aβ amyloid fibrils, leading to the activation of inflammatory signaling cascades [10].

Under physiological conditions, lipid-free apoC-II spontaneously forms homogeneous twisted-ribbon fibrils with all of the hallmarks of amyloid fibrils including a cross-β structure and the ability to bind Congo red and Thioflavin T [11, 12]. A range of physical methods have been used to characterize the structure of the twisted-ribbon fibrils formed by lipid-free apoC-II [12]. The model proposes a single apoC-II molecule in a “letter G” configuration with the cross-β structure composed of N- and C-terminal regions that form an outer and inner β-sheet, respectively. An important feature of this model is the presence of a buried charge-pair between K30 and D69 residues. This ion pair accounts for the apparent paradox that apoC-II can adopt an

amphipathic α-helical structure in the presence of phospholipid with polar residues aligned on one side of the helix and a cross-β structure in the lipid-free state where residues alternate between solvent exposed and buried positions [13].

Studies on the effects of lipids on apoC-II show that high concentrations of micellar or vesicular phospholipids completely inhibit fibril formation [14, 15]. However, in the presence of low concentrations of micellar or vesicular phospholipids, fibril formation is only partly inhibited with a two-phase growth pattern leading to the formation of fibrils with a distinct straight, rod-like morphology and displaying all of the hallmarks of amyloid fibrils [15]. Such structural polymorphisms are common for other amyloid systems [16] including Aβ fibrils [17, 18] where the different morphologies show differing toxicities, and PrP where molecular-level polymorphisms provide the underlying mechanism for distinct prion strains [19]. Currently, little is known about the properties of the two distinct fibril morphologies exhibited by apoC-II. Mutations of the charge-pair residues K30 and D69 exert significant effects on the rate of formation and stability of twisted ribbon fibrils [13, 20, 21]. We explored the effect of these mutations on the rate of formation of rod-like apoC-II fibrils. We have also applied several biophysical methods to develop a structural model for rod-like apoC-II fibrils which permits a comparison with the existing model for twisted-ribbon apoC-II fibrils [12].

Results

The effect of mutations on rod-like apoC-II fibril formation

Previous structural and mutational studies of twisted-ribbon apoC-II fibrils identified a buried K30-D69 ion pair that linked the N- and C-terminal regions of apoC-II and modulated both the rate of fibril formation and fibril stability [13, 20-22]. It was therefore of interest to determine the effect of the mutations in this ion pair on rod-like fibril formation. The results in Figure 1 show the rate of fibril formation by wild-type apoC-II (WT) and three apoC-II mutants, K30D, D69K and the double mutant K30D, D69K (KDDK) in the absence and presence of 500 μM 1-Myristoyl-2-Hydroxy-*sn*-Glycero-3-Phosphocholine (LysoMPC). As previously reported, twisted-ribbon fibril formation by lipid-free WT, D69K and KDDK apoC-II is rapid while fibril formation by K30D apoC-II under these conditions is comparatively slow [20]. The observed

differences in the fluorescence yields of WT and mutant apoC-II are attributable to differences in the net charge of the fibrils [20]. The rates of apoC-II rod-like fibril formation in the presence of 500 μM LysoMPC differed significantly. The initial stages of rod-like fibril formation by WT, D69K and K30D apoC-II were inhibited while over an extended period of time (400-600 h) thioflavin T (ThT) fluorescence increased to higher levels than those observed in the absence of LysoMPC. This increase is consistent with the formation of rod-like fibrils that have previously been shown to have a higher ThT fluorescence yield compared to twisted-ribbon fibrils [15]. The results in Figure 1B indicate the rate of rod-like fibril formation by D69K apoC-II is similar to WT, whereas a slower increase in rod-like fibril formation is observed for K30D apoC-II. The results obtained for fibril formation by KDDK apoC-II in the presence of 500 μM LysoMPC were similar to those for KDDK apoC-II in the absence of phospholipid. Very little inhibition was observed at the early stages of incubation and the plateau levels of ThT fluorescence obtained after prolonged incubation were similar to those observed in the absence of phospholipid.

Electron microscopy analysis of rod-like apoC-II fibrils

Transmission electron microscopy studies using negative staining confirmed the formation of rod-like fibrils by WT, D69K and K30D apoC-II after prolonged incubation in the presence of 500 μM LysoMPC (Figure 2). Electron micrographs of fibrils formed by KDDK apoC-II in the presence of 500 μM LysoMPC for the same period revealed some rod-like fibril formation, but a majority of twisted ribbon fibrils (Figure 2G-H). Analysis of the negatively stained images indicated variation in the width of fibrils, although no significant differences between WT (7.9 ± 1.3 nm), K30D (10.0 ± 1.7 nm), D69K (11.0 ± 2.3 nm), and KDDK (8.9 ± 2.0 nm) fibril widths were observed (measurements are mean ± SD; $n > 120$). This variation may indicate a lack of cylindrical symmetry or differences in the depth of the negative stain in different regions of the grid. The periods of the regular helical twist evident in the fibril long axis were WT (98.2 ± 12.3 nm), K30D (91.5 ± 6.4 nm), D69K (93.5 ± 7.0 nm), and KDDK (93.3 ± 8.6 nm), showing closer agreement between the variants (mean ± SD; $n > 10$).

Cross seeding of rod-like apoC-II fibril formation

A characteristic property of rod-like apoC-II fibrils is the ability of small seeds, obtained by freeze-fracture, to accelerate or seed rod-like fibril formation by apoC-II in either the presence or

absence of added phospholipid [15]. Seeding experiments were conducted to investigate whether fibril seeds obtained from WT, K30D or D69K rod-like fibrils could seed the formation of rod-like fibrils by other apoC-II mutants. Electron micrographs of seeds obtained by freeze-thawing of WT, D69K and K30D apoC-II rod-like fibrils revealed rod-like fibril seeds with typical lengths in the range 20-80 nm, as reported previously [15]. These seeds were incubated (2% w/w of the total protein) with WT, D69K, K30D and KDDK apoC-II monomer at 1 mg/mL, in the presence of 500 μM LysoMPC. The results of ThT fluorescence monitoring showed that WT apoC-II monomer undergoes an accelerated second aggregation phase in the presence of WT, D69K and K30D apoC-II seeds (Figure 3) compared to the absence of seeds (Figure 1). The higher plateau levels of ThT florescence, compared to fibrils grown in the absence of LysoMPC (Figure 1), are indicative of the formation of rod-like fibrils [15]. Similar results were obtained using WT, D69K and K30D apoC-II seeds added to either D69K or K30D monomers, where accelerated fibril formation compared with non-seeded fibril formation and higher plateau levels of ThT fluorescence was observed, consistent with the formation of rod-like fibrils. These results may be contrasted with the results for the KDDK apoC-II monomer where the addition of WT, D69K and K30D apoC-II seeds generated a much slower increase in ThT fluorescence and lower overall levels after prolonged incubation confirming the reduced ability of KDDK apoC-II to form rod-like apoC-II fibrils. The increases observed indicate WT and D69K seeds are more effective than K30D seeds in promoting KDDK fibril formation. Notwithstanding the lower overall ThT fluorescence development with the seeded KDDK apoC-II fibril incubations, electron micrographs of the products formed revealed extensive formation of rod-like KDDK fibrils with average lengths in the 100-300 nm size range (Figure 4).

Hydrogen/Deuterium exchange studies

Hydrogen/Deuterium (H/D) exchange coupled with NMR studies have been used previously to develop a structural model for twisted-ribbon apoC-II fibrils [12]. This method was applied to the analysis of rod-like apoC-II fibrils. Two-dimensional (2D) ^{1}H-^{15}N SOFAST HMQC NMR spectra for rod-like fibril samples exposed to D_2O over 24 h as well as protonated reference samples are presented in Figure 5A and 5B, respectively. The amide proton assignments shown are based on sequential resonance assignments of ^{13}C, ^{15}N-apoC-II reported previously [23]. The results show retention of resonances arising from the C-terminal region of apoC-II following

D_2O exposure. This H/D exchange protection is displayed in Figure 5C as the ratio of signal intensity relative to the protonated reference sample. Strong protection is observed for residues 58-76. These results may be compared to previous results for twisted ribbon fibrils where protection was observed for both the (19-37) N-terminal region and (57-74) C-terminal region [23]. The results indicate that the cross-β structure of rod-like apoC-II fibrils is composed solely of the C-terminal region, in contrast to the G-like structure of twisted-ribbon fibrils composed of both N- and C-terminal regions. The observed continuity of amide proton exchange protection throughout this region suggests that residues 58-76 form one continuous β-strand and do not contain any turn structure. These results imply that at least two apoC-II molecules are included per rise of the cross-β sheet.

Acrylamide quenching analysis

The lack of H/D exchange protection in the N-terminal region of rod-like apoC-II fibrils raised the question of whether this region was structurally disordered. Acrylamide fluorescence quenching experiments were performed to determine the accessibility of W26 to solvent. Stern-Volmer plots (Figure 6) show strong acrylamide quenching of W26 in freshly prepared apoC-II characterized by a quenching constant of 9.7 ± 0.1 while acrylamide quenching for twisted-ribbon and rod-like fibrils was significantly lower with quenching constants of 4.2 ± 0.1 and 3.5 ± 0.1, respectively. These results indicate that while the N-terminal region of rod-like fibrils displays low H/D exchange protection, residue W26 was protected from solvent and in a buried location.

Molecular Dynamics simulations of apoC-II 56-76 peptide fibrils

The results of the H/D exchange analysis of rod-like fibrils indicate strong protection by residues 58-76 consistent with a cross-β structure comprising adjacent apoC-II molecules with at least two molecules per rise of the β-sheets. Molecular dynamics (MD) simulations were carried out to estimate the relative stabilities of parallel and antiparallel orientations of peptide fibrils composed of apoC-II (56-76), a peptide sequence we have previously shown to spontaneously form amyloid fibrils [24]. Three starting arrangements of the β-strands for both parallel and anti-parallel configurations were considered (Figure 7).

Starting arrangements 1, 2 and 3 were distinguished by the exposure of the charged D69 residues on the outside of the cross-β sheet of 1, 0 and 2, respectively. The results of the MD simulations show parallel arrangement 3 preserved the highest amount of β-structure for the middle four subunits of the fibril with a cluster population of 74% (Figure 8) and average inter-sheet spacing of 10.4 ± 1.9 Å . Of the anti-parallel arrangements, only arrangement 3 preserved appreciable β-structure with a cluster population of 35%. Overall, the MD results indicate as favourable the parallel arrangement 3 of the C-terminal region in rod-like apoC-II fibrils with some distortion of the β-content in the region 68-76. This distortion is attributable to the effects of the charged residue K76, an effect that may be reduced in the full-length protein by the presence of the negatively charged Glu residues at positions 78 and 79. These results are consistent with sequence based predictions from PASTA 2.0 [25], where the ten lowest energy self-pairing sequences from calculations using the complete apoC-II sequence comprised parallel arrangements of 4-16 residue segments spanning positions 60-76.

X-ray diffraction analysis

X-ray diffraction data for aligned rod-like apoC-II fibrils are presented in Figure 9. The diffraction pattern is typical of a cross-β structure with dominant orthogonal reflections on the meridional and equatorial axes [26]. Analysis of the data shows major peaks on the meridional and equatorial axis with spacings of 4.60 ± 0.01 Å and 9.69 ± 0.01 Å, respectively (Table 1). These values correspond to the spacings between the β-strands of each β-sheet and between the β-sheets in the cross section of the cross-β structure. The values can be compared to values for meridional and equatorial spacings of 4.65 ± 0.01 Å and 9.57 ± 0.02 Å respectively previously reported for aligned twisted-ribbon apoC-II amyloid fibrils [21]. Thus, both the meridional and equatorial spacings are different for the twisted-ribbon and rod-like fibrillar structures. The two longer equatorial spacings (23.8 Å and 46.6 Å) for rod-like fibrils are not observed in X-ray diffraction patterns for aligned twisted-ribbon fibrils [12, 21] and suggest the presence of more than two β-sheets in the fibril cross section.

As fibre diffraction data suggested more than two β-sheets in the fibril cross section, arrangements of multiple units of parallel arrangement 3 (Figure 7) were explored, and simulated X-ray diffraction patterns were calculated and compared to the experimental diffraction data

(Figure 9). Two units of the parallel arrangement 3 starting structure arranged in the fibril cross section as in Figure 9B provided the closest fit to the experimental diffraction pattern (Figure 9A, lower left quadrant). In particular, two lower resolution reflections in the calculated diffraction pattern result from this configuration at similar positions to those observed in the experimental data, and these are not observed for a single cross-β unit. Considerations of the spatial packing of the two units together and the exposure of the D69, suggested that the two units would most likely take an antiparallel configuration with respect to each other. Thus, this configuration of the cross-β structure in the fibril cross section provides a model of the fibril core structure that is consistent with our biophysical data.

Discussion

Rod-like and twisted-ribbon apoC-II fibrils differ considerably in their morphologies but exhibited broadly similar X-ray diffraction patterns consistent with their inherent cross-β structure, a defining characteristic of amyloid fibrils. Morphological analysis of rod-like fibrils showed they are essentially cylindrical in nature with widths of approximately 8-11 nm and a regular helical twist period of around 90-100 nm, consistent with previous data [15]. In contrast, twisted ribbon fibrils display widths of approximately 12 nm and ribbon thickness of about 2 nm determined from atomic force microscopy [12]. A major difference between twisted-ribbon and rod-like apoC-II fibrils was detected by H/D exchange experiments. For twisted ribbon fibrils, H/D exchange protection was observed in both N- and C-terminal regions. This protection pattern is consistent with a G-like subunit structure with a rise of one apoC-II subunit per β-strand interval where the N- and C-terminal regions form separate parallel β-sheets of parallel strands connected by a flexible loop [12]. In contrast, our H/D exchange data for rod-like fibrils indicated protection is limited to the C-terminal region, implying at least two apoC-II molecules per β-strand rise. Cylindrical models involving 2, 3, or 4 tightly packed apoC-II molecules per β-strand rise, have calculated fibril widths of approximately 7.65, 9.37 and 10.8 nm, respectively. The widths of rod-like fibrils estimated from analysis of negative staining electron microscopy images lie in the range 8-11 nm. This wide variation, together with the uncertainties in fibril cross-section shape, conformation and position of the N-terminal part of the protein, and depth of the negative stain in different regions of the grid do not allow a distinction between models involving 2, 3 or 4 apoC-II units per rise of the β-sheet.

Our model for rod-like fibrils comprises four apoC-II molecules per rise, consistent with the long equatorial spacings observed in our fibre diffraction data. This configuration has significant implications for the assembly of rod-like fibrils. For twisted-ribbon amyloid fibrils, where there is one molecule per rise of the β-sheet, a simple subunit self-association mechanism adequately describes the kinetics of fibril formation [27]. Since twisted-ribbon fibrils involve both N- and C-terminal β-sheets it is unlikely that twisted-ribbon fibrils represent an intermediate in the formation of rod-like fibrils. A more likely assembly mechanism would be initial dimer formation via interactions between the C-terminal regions of two apoC-II molecules forming an amyloidogenic nucleus that serves as a starting point for subunit addition and fibril growth. This mechanism would explain the action of low concentrations of lipid micelle and vesicle surfaces in promoting rod-like fibril formation since apoC-II subunits concentrated at the lipid surface would facilitate dimer formation. Similarly, the acceleration of rod-like apoC-II fibril formation by short rod-like fibril seeds would provide a nucleus to circumvent the need for an initial sub-unit dimerization.

The time-dependent formation of rod-like fibrils by WT, K30D and D69K apoC-II contrasts with the inability of the double mutant, KDDK apoC-II to form rod-like fibrils under the same conditions. An explanation for this observation is that the K30D mutation occurs in a lipid-binding region of apoC-II [28], limiting the ability of this mutant to bind to the lipid surface and initiate dimerization and subsequent fibril elongation. Such an effect would also limit rod-like fibril formation by the single mutant, K30D apoC-II. Indeed, rod-like fibril formation by K30D apoC-II is slower than that observed for WT and D69K apoC-II. An extenuating circumstance arises in the case of K30D apoC-II which has a significantly reduced ability to form twisted-ribbon fibrils [13]. This competing pathway, available to KDDK apoC-II, would also further limit the ability of the double mutant to form rod-like fibrils. The observation that WT, K30D or D69K apoC-II fibril seeds promote the formation of KDDK rod-like fibrils is consistent with this explanation since the seeds would bypass the need for KDDK apoC-II to bind initially to a lipid surface.

The model we propose for rod-like apoC-II amyloid fibrils extends the list of stable conformations adopted by the protein. NMR analysis of apoC-II in the presence of sodium dodecyl sulphate or dodecylphosphocholine micelles has defined a predominantly α-helical structure, with helices located in both the N- and C-terminal regions of the molecule [29, 30]. A

well-defined apoC-II dimer forms in the presence of submicellar concentrations of sodium dodecylphosphocholine [31]. In addition to these conformations, apoC-II spontaneously forms homogeneous twisted-ribbon fibrils in the absence of lipids and rod-like fibrils in the presence of low concentrations of micellar lipids. The conformational flexibility of apoC-II may be a common feature of the apolipoprotein family where specific and discrete structures form. This structural metamorphism could determine the fate of apoC-II in amyloid deposits and underlie the observed association between apoC-II plasma levels and the risk of cardiovascular disease.

Materials and methods

Expression and purification of apoC-II

The pET-11a expression plasmid containing WT apoC-II, K30D, D69K and the double mutant (K30D, D69K) apoC-II (KDDK)were purified by Miniprep (Qiagen Inc., MD) and transformed into *Escherichia coli* BL21(DE3) for expression and purification as described previously [11, 20]. ^{15}N labeled WT apoC-II was expressed and purified using the protocol previously described [32, 33]. Purified apoC-II preparations were stored as 30 - 40 mg/mL stocks at -20 °C in 5 M guanidine hydrochloride (GuHCl) and 10 mM Tris.HCl, pH 8.0.

ApoC-II fibril formation

ApoC-II fibril formation was initiated by diluting protein stock into sodium phosphate buffer (100 mM sodium phosphate, 0.1% (w/v) sodium azide, at pH 7.4), to a final concentration of 1 mg/mL, either in the absence or presence of 500 μM LysoMPC. Samples were incubated at 20 °C to allow the formation of amyloid fibrils.

Rod-like fibrils were also obtained using seeds of pre-formed rod-like fibril as templates to elongate apoC-II monomer into fibrils. Mature rod-like fibrils were separated from twisted ribbon fibrils by centrifugation at 14,500 g for 2 min. Twisted ribbon fibrils do not sediment appreciably under these conditions. The pellet was then resuspended in an equal volume of refolding buffer containing 500 μM LysoMPC at pH 7.4. The process was repeated three times to optimize the purity of rod-like fibrils. Isolated rod-like fibrils were fragmented by freezing in liquid nitrogen and thawing in a water bath at 25 ºC. Seven freeze-thaw cycles were employed. The concentration of the rod-like fibril seeds prepared in this way was in the range of 0.7- 0.85 mg/ml. Rod-like fibril formation via template was initiated by adding 2% seeds (w/w final total

protein concentration) and protein stock into refolding buffer with 500 μM LysoMPC at pH 7.4, to a final concentration of 1 mg/mL.

^{15}N labelled apoC-II protein stocks were exchanged into refolding buffer using a NAP 5 desalting column (GE Healthcare-Amersham Biosciences, Piscataway, NJ, USA) to remove residual GuHCl. Rod-like fibril formation was initiated by adding WT apoC-II seeds (2% w/w final total protein concentration, prepared as described above) to ^{15}N labelled apoC-II in refolding buffer with 500 μM LysoMPC at pH 7.4, to a final concentration of 1 mg/mL and incubated at 20 ºC for 7 days.

Thioflavin T fluorescence assays

ThT purchased from Sigma (MO, USA) was used to monitor amyloid fibril formation [34, 35]. Aliquots (20 μL) of incubation mixtures were mixed with ThT in a 96-well microtiter plate well to give a final concentration of 10 μM ThT in phosphate buffer and a final volume of 250 μL. The presence of lipids in the incubation mixtures had no significant effect on ThT fluorescence. Fluorescence intensities were measured using an f_{max} fluorescence plate reader with excitation and emission filters of 444 and 485 nm, respectively. Measurements were made in duplicate.

Transmission Electron Microscopy

Carbon-coated copper grids were glow discharged for 15 sec prior to sample application. ApoC-II fibril samples were diluted with distilled water to 0.1 mg/mL, applied to grids, and allowed to adsorb for 1 min. Samples were then blotted from the grid, stained twice with 2% potassium phosphotungstate, pH 6.8, and air-dried. Grids were examined at the Bio21 Electron Microscopy Unit using a FEI Tecnai G2 TF20 transmission electron microscope (FEI-Company, Eindhoven, The Netherlands), and a Gatan US1000 2k×2k CCD Camera (Pleasanton, CA, USA) was used to acquire digital images.

Hydrogen/Deuterium exchange analysis

H/D exchange experiments were performed as previously described [23]. Briefly, rod-like ^{15}N labeled apoC-II fibril samples were collected by centrifugation at 100,000 rpm for 30 min (MLA 130 rotor, OptimaMax centrifuge, USA). A batch of pellet obtained from an aliquot sample of 500 μl was kept separate for acquiring a ^{1}H-^{15}N SOFAST HMQC reference spectrum for the fully protonated sample. This pellet was immediately snap-frozen in liquid nitrogen and stored at

-20 °C. To initiate deuterium incorporation, the remaining fractions were resuspended in 2.5 mM Tris-HCl buffer, 100% D_2O, pH 7.4 (uncorrected glass electrode reading) and incubated at 20 °C. After 24 h the fibrils were collected by centrifugation at 100,000 rpm for 30 min and the resulting pellet was kept at -20 °C. Prior to transfer to an NMR tube, the frozen pellets were solubilized in a solution containing 95% (v/v) d_6-dimethyl sulphoxide (DMSO), 4.5% D_2O (or H_2O for the protonated reference sample), 0.5% d_2-dichloroacetic acid (d_2-DCA), pH 4.3 (uncorrected glass electrode reading). Measurements were performed on a Bruker 800 MHz Avance II NMR spectrometer. Two-dimensional ^{1}H-^{15}N SOFAST HMQC spectra [36]were obtained at 25 ºC using a spectral width of 10504 Hz and 2048 data points in the ^{1}H dimension, and a spectral width of 1621 Hz in the ^{15}N dimension with 256 t_1 increments with 16 transients per t_1 point. The ^{1}H variable flip-angle PC9 shaped pulse [37] was 2.25 ms and the ^{1}H band-selective refocusing r-SNOB pulse [38] was 1 ms. The relaxation delay between transients was 0.3 s. Data was also collected for a reference protonated sample dissolved in the same buffer. Data were processed using NMRPipe [39] and analyzed in NMRView [40].

Fluorescence quenching analysis

Fluorescence quenching experiments were conducted using a Cary Varian Eclipse Fluorescence Spectrophotometer (Agilent Technologies) at 20 ºC using acrylamide as an external quencher. The excitation and emission wavelengths were set at 295 nm and 344 nm, respectively. Data was obtained for freshly prepared apoC-II and for samples (1 mg/ml) incubated in sodium phosphate refolding buffer, pH 7.4, at 20 ºC for 750 h in the absence or presence of 500 μM LysoMPC. Serial additions of acrylamide (2 μL of 2 M) were added to the apoC-II samples (0.05 mg/ml) and the effective quenching constants calculated as described previously [12].

Molecular Dynamics simulations

Explicit solvent MD simulations were performed to examine the conformational stability of pre-formed apoC-II (56-76) fibril 12-mers. This is the region with the showed highest H/D exchange protection and the ability to form fibrils independently [23]. Three different parallel and anti-parallel arrangements of a straight fibril composed of two apoC-II (56-76) molecules per rise joined in a cross-β structure (with ~4.8 Å distance between the β-strands and ~10-11 Å intersheet

separation) were constructed using the Biovia Discovery Studio Visualizer [41]. The peptides were modelled in an extended conformation with the N- and C-termini capped with acetyl and amide groups respectively. The six different starting arrangements are shown in Figure 7.

All simulations were performed using GROMACS 5.1.2 modelling suite [42], with the same simulation parameters and system setup approach used in our previous studies [22, 43]. The protein and water pairwise interactions were modelled using the GROMOS 43A1 forcefield parameter set [44] and SPC water model [45]. Cross-cell interactions were prevented by placing each 12-mer fibril in a large cubic periodic box with 12 Å minimal distance between the solute and edges of the box. The simulation box was then solvated to water density of ~1.0 g/cm^3. Initial energy minimization was performed using the steepest descent approach to remove any steric clashes. To relax the solvent around the protein a short 100 ps MD simulation was conducted with the fibril restrained. Unrestrained NPT (constant number of particles, pressure and temperature) MD simulations were performed for 150 ns for each system, and a total of 900 ns of data was collected. The total energy and root-mean-square deviation (RMSD) were monitored as a measure of equilibration, and the last 50 ns of simulations was used for analysis for each system.

Secondary structure analysis and visualization of the trajectories was done using the visual molecular dynamics (VMD) software [46]. To take into consideration any conformational variations and exclude the fraying/disordered ends, the secondary structure of the middle four subunits from each 12-mer were calculated using the STRIDE algorithm, and the data were averaged from the four subunit arrangements. Similarly, the inter-sheet spacing of the favored parallel arrangement was measured from the middle four subunits by taking the average of the backbone α-carbon separations of opposing (facing) residues A59-I66, the region of highest β-strand content and stability in the arrangements examined.

X-ray diffraction

Rod-like fibrils were pelleted by centrifugation at 100,000 rpm for 30 min using an OptimaMax centrifuge and a TLA-100 rotor (Beckman Coulter Instruments, Inc., Fullarton, CA, USA), followed by resuspension in distilled water. Centrifugation and resuspension were repeated three times to remove buffer salts. Finally, the fibril pellet was resuspended in a small volume of distilled water, to a concentration of approximately 10 mg/ml. Fibrils were aligned using a

modification of the stretch frame method [47] in which the distance between wax-tipped capillaries is held constant during the drying of the fibril suspension droplet. X-ray diffraction images were acquired at the Australian Synchrotron MX2 beamline operating at 13.0 keV (λ = 0.954 Å). The sample-to-detector distance was 200 mm, and the exposure time was 10 s. Diffraction images were analysed using the software package CLEARER [48]. Simulated diffraction patterns were calculated using CLEARER [48] by constructing models of the fibril cross section using varying numbers and arrangements of the energy minimised starting structure for parallel arrangement 3 (see Figure 7). Lattice vectors were set accordingly, with the vector in the fibril long-axis maintained at 4.60 Å. Angular fibril disorder was 0.4 radians and the crystallite size was 100 Å, 500 Å, 50 Å, corresponding to a short fibril and consistent with measured fibril widths.

Acknowledgements

M.D.W.G is the recipient of an Australian Research Council Future Fellowship (project number FT140100544). I.Y and N.T. acknowledge the support from the NHMRC Centre of Research Excellence for Electromagnetic Bioeffects Research (CRE1042464). This research was undertaken with the assistance of resources from the National Computational Infrastructure (NCI, grant e87) and Melbourne Bioinformatics Facility, an initiative of the Victorian Government, Australia. Parts of this research were undertaken at the MX2 beam-line of the Australian Synchrotron, Victoria, Australia.

Author contributions

G.J.H., I.Y., P.R.G., and M.D.W.G. designed the study; C.O.Z., Y.M., N.T., Y-F.M., and M.D.W.G. performed the experiments; C.O.Z., Y.M., N.T., Y-F.M., G.J.H., I.Y., P.R.G., and M.D.W.G. analysed the data; C.O.Z., Y.M., N.T., G.J.H., and M.D.W.G. wrote the manuscript with input from Y-F.M., I.Y., and P.R.G.

References

1. Kinnunen, P. K., Jackson, R. L., Smith, L. C., Gotto, A. M., Jr. & Sparrow, J. T. (1977) Activation of lipoprotein lipase by native and synthetic fragments of human plasma apolipoprotein C-II, *Proc Natl Acad Sci U S A.* **74**, 4848-51.
2. Pechlaner, R., Tsimikas, S., Yin, X., Willeit, P., Baig, F., Santer, P., Oberhollenzer, F., Egger, G., Witztum, J. L., Alexander, V. J., Willeit, J., Kiechl, S. & Mayr, M. (2017) Very-Low-Density Lipoprotein-Associated Apolipoproteins Predict Cardiovascular Events and Are Lowered by Inhibition of APOC-III, *J Am Coll Cardiol.* **69**, 789-800.
3. Nasr, S. H., Dasari, S., Hasadsri, L., Theis, J. D., Vrana, J. A., Gertz, M. A., Muppa, P., Zimmermann, M. T., Grogg, K. L., Dispenzieri, A., Sethi, S., Highsmith, W. E., Jr., Merlini, G., Leung, N. & Kurtin, P. J. (2017) Novel Type of Renal Amyloidosis Derived from Apolipoprotein-CII, *J Am Soc Nephrol.* **28**, 439-445.
4. Sethi, S., Dasari, S., Plaisier, E., Ronco, P., Nasr, S. H., Brocheriou, I., Theis, J. D., Vrana, J. A., Zimmermann, M. T., Quint, P. S., McPhail, E. D. & Kurtin, P. J. (2018) Apolipoprotein CII amyloidosis associated with p.Lys41Thr mutation, *Kidney International Reports.* **doi: 10.1016/j.ekir.2018.04.009.**
5. Teoh, C. L., Griffin, M. D. & Howlett, G. J. (2011) Apolipoproteins and amyloid fibril formation in atherosclerosis, *Protein Cell.* **2**, 116-27.
6. Sipe, J. D., Benson, M. D., Buxbaum, J. N., Ikeda, S. I., Merlini, G., Saraiva, M. J. & Westermark, P. (2016) Amyloid fibril proteins and amyloidosis: chemical identification and clinical classification International Society of Amyloidosis 2016 Nomenclature Guidelines, *Amyloid.* **23**, 209-213.
7. Hatters, D. M. & Howlett, G. J. (2002) The structural basis for amyloid formation by plasma apolipoproteins: a review, *Eur Biophys J.* **31**, 2-8.
8. Stewart, C. R., Haw, A., 3rd, Lopez, R., McDonald, T. O., Callaghan, J. M., McConville, M. J., Moore, K. J., Howlett, G. J. & O'Brien, K. D. (2007) Serum amyloid P colocalizes with apolipoproteins in human atheroma: functional implications, *Journal of lipid research.* **48**, 2162-71.
9. Medeiros, L. A., El Khoury, J. B., Pham, C. L., Hatters, D. M., Howlett, G. J., O'Brien, K. D. & Moore, K. J. (2004) Fibrillar amyloid proteins present in human atheroma activate CD36-signal transduction, *Arterioscl Throm Vas.* **24**, E26-E26.

10. Howlett, G. J. & Moore, K. J. (2006) Untangling the role of amyloid in atherosclerosis, *Curr Opin Lipidol.* **17**, 541-7.
11. Hatters, D. M., MacPhee, C. E., Lawrence, L. J., Sawyer, W. H. & Howlett, G. J. (2000) Human apolipoprotein C-II forms twisted amyloid ribbons and closed loops, *Biochemistry.* **39**, 8276-83.
12. Teoh, C. L., Pham, C. L., Todorova, N., Hung, A., Lincoln, C. N., Lees, E., Lam, Y. H., Binger, K. J., Thomson, N. H., Radford, S. E., Smith, T. A., Muller, S. A., Engel, A., Griffin, M. D., Yarovsky, I., Gooley, P. R. & Howlett, G. J. (2011) A Structural Model for Apolipoprotein C-II Amyloid Fibrils: Experimental Characterization and Molecular Dynamics Simulations, *J Mol Biol.* **405**, 1246-1266.
13. Mao, Y., Todorova, N., Zlatic, C. O., Gooley, P. R., Griffin, M. D., Howlett, G. J. & Yarovsky, I. (2016) Solution conditions affect the ability of K30D mutation to prevent amyloid fibril formation by apolipoprotein C-II: insights from experiments and theoretical simulations, *Biochemistry*.
14. Hatters, D. M., Lawrence, L. J. & Howlett, G. J. (2001) Sub-micellar phospholipid accelerates amyloid formation by apolipoprotein C-II, *FEBS Lett.* **494**, 220-4.
15. Griffin, M. D., Mok, M. L., Wilson, L. M., Pham, C. L., Waddington, L. J., Perugini, M. A. & Howlett, G. J. (2008) Phospholipid interaction induces molecular-level polymorphism in apolipoprotein C-II amyloid fibrils via alternative assembly pathways, *J Mol Biol.* **375**, 240-56.
16. Tycko, R. (2015) Amyloid polymorphism: structural basis and neurobiological relevance, *Neuron.* **86**, 632-45.
17. Moore, R. A., Hayes, S. F., Fischer, E. R. & Priola, S. A. (2007) Amyloid formation via supramolecular peptide assemblies, *Biochemistry.* **46**, 7079-87.
18. Petkova, A. T., Leapman, R. D., Guo, Z., Yau, W. M., Mattson, M. P. & Tycko, R. (2005) Self-propagating, molecular-level polymorphism in Alzheimer's beta-amyloid fibrils, *Science.* **307**, 262-5.
19. Collinge, J. & Clarke, A. R. (2007) A general model of prion strains and their pathogenicity, *Science.* **318**, 930-6.
20. Mao, Y., Teoh, C. L., Yang, S., Zlatic, C. O., Rosenes, Z. K., Gooley, P. R., Howlett, G. J. & Griffin, M. D. W. (2015) Charge and charge-pair mutations alter the rate of assembly and structural properties of apolipoprotein C-II amyloid fibrils, *Biochemistry.* **54**, 1421-8.

21. Mao, Y., Zlatic, C. O., Griffin, M. D., Howlett, G. J., Todorova, N., Yarovsky, I. & Gooley, P. R. (2015) Hydrogen/Deuterium Exchange and Molecular Dynamics Analysis of Amyloid Fibrils Formed by a D69K Charge-Pair Mutant of Human Apolipoprotein C-II, *Biochemistry*.
22. Todorova, N., Zlatic, C. O., Mao, Y., Yarovsky, I., Howlett, G. J., Gooley, P. R. & Griffin, M. D. W. (2017) Intra- and Intersubunit Ion-Pair Interactions Determine the Ability of Apolipoprotein C-II Mutants To Form Hybrid Amyloid Fibrils, *Biochemistry.* **56**, 1757-1767.
23. Wilson, L. M., Mok, Y. F., Binger, K. J., Griffin, M. D., Mertens, H. D., Lin, F., Wade, J. D., Gooley, P. R. & Howlett, G. J. (2007) A structural core within apolipoprotein C-II amyloid fibrils identified using hydrogen exchange and proteolysis, *J Mol Biol.* **366**, 1639-51.
24. Legge, F. S., Binger, K. J., Griffin, M. D. W., Howlett, G. J., Scanlon, D., Treutlein, H. & Yarovsky, I. (2009) Effect of Oxidation and Mutation on the Conformational Dynamics and Fibril Assembly of Amyloidogenic Peptides Derived from Apolipoprotein C-II, *J Phys Chem B.* **113**, 14006-14014.
25. Walsh, I., Seno, F., Tosatto, S. C. & Trovato, A. (2014) PASTA 2.0: an improved server for protein aggregation prediction, *Nucleic acids research.* **42**, W301-7.
26. Sunde, M., Serpell, L. C., Bartlam, M., Fraser, P. E., Pepys, M. B. & Blake, C. C. (1997) Common core structure of amyloid fibrils by synchrotron X-ray diffraction, *J Mol Biol.* **273**, 729-39.
27. Binger, K. J., Pham, C. L., Wilson, L. M., Bailey, M. F., Lawrence, L. J., Schuck, P. & Howlett, G. J. (2008) Apolipoprotein C-II amyloid fibrils assemble via a reversible pathway that includes fibril breaking and rejoining, *J Mol Biol.* **376**, 1116-29.
28. MacPhee, C. E., Howlett, G. J., Sawyer, W. H. & Clayton, A. H. A. (1999) Helix-helix association of a lipid-bound amphipathic alpha-helix derived from apolipoprotein C-II, *Biochemistry.* **38**, 10878-10884.
29. MacRaild, C. A., Hatters, D. M., Howlett, G. J. & Gooley, P. R. (2001) NMR structure of human apolipoprotein C-II in the presence of sodium dodecyl sulfate, *Biochemistry.* **40**, 5414-21.
30. MacRaild, C. A., Howlett, G. J. & Gooley, P. R. (2004) The structure and interactions of human apolipoprotein C-II in dodecyl phosphocholine, *Biochemistry.* **43**, 8084-93.
31. Ryan, T. M., Griffin, M. D. W., McGillivray, D. J., Knott, R. B., Wood, K., Masters, C. L., Kirby, N. & Curtain, C. C. (2016) Apolipoprotein C-II Adopts Distinct Structures in Complex

with Micellar and Submicellar Forms of the Amyloid-Inhibiting Lipid-Mimetic Dodecylphosphocholine, *Biophys J.* **110**, 85-94.
32. Cai, M., Huang, Y., Sakaguchi, K., Clore, G. M., Gronenborn, A. M. & Craigie, R. (1998) An efficient and cost-effective isotope labeling protocol for proteins expressed in Escherichia coli, *J Biomol NMR.* **11**, 97-102.
33. Marley, J., Lu, M. & Bracken, C. (2001) A method for efficient isotopic labeling of recombinant proteins, *J Biomol NMR.* **20**, 71-5.
34. Saeed, S. M. & Fine, G. (1967) Thioflavin-T for amyloid detection, *Am J Clin Pathol.* **47**, 588-93.
35. Naiki, H., Higuchi, K., Hosokawa, M. & Takeda, T. (1989) Fluorometric determination of amyloid fibrils in vitro using the fluorescent dye, thioflavin T1, *Anal Biochem.* **177**, 244-9.
36. Schanda, P. & Brutscher, B. (2005) Very fast two-dimensional NMR spectroscopy for real-time investigation of dynamic events in proteins on the time scale of seconds, *Journal of the American Chemical Society.* **127**, 8014-5.
37. Kupce, E. & Freeman, R. (1993) Polychromatic Selective Pulses, *J Magn Reson Ser A.* **102**, 122-126.
38. Kupce, E., Boyd, J. & Campbell, I. D. (1995) Short selective pulses for biochemical applications, *Journal of magnetic resonance Series B.* **106**, 300-3.
39. Delaglio, F., Grzesiek, S., Vuister, G. W., Zhu, G., Pfeifer, J. & Bax, A. (1995) NMRPipe: a multidimensional spectral processing system based on UNIX pipes, *J Biomol NMR.* **6**, 277-93.
40. Johnson, B. A. & Blevins, R. A. (1994) NMR View: A computer program for the visualization and analysis of NMR data, *J Biomol NMR.* **4**, 603-14.
41. (2016) Discovery Studio Modeling Environment Release 2017 in, Dassault Systèmes BIOVIA, San Diego: Dassault Systèmes.
42. Abraham, M. J., Murtola, T., Schulz, R., Páll, S., Smith, J. C., Hess, B. & Lindahl, E. (2015) GROMACS: High performance molecular simulations through multi-level parallelism from laptops to supercomputers, *SoftwareX.* **1-2**, 19-25.
43. Mao, Y., Todorova, N., Zlatic, C. O., Gooley, P. R., Griffin, M. D., Howlett, G. J. & Yarovsky, I. (2016) Solution Conditions Affect the Ability of the K30D Mutation To Prevent Amyloid Fibril Formation by Apolipoprotein C-II: Insights from Experiments and Theoretical Simulations, *Biochemistry.* **55**, 3815-24.

44. van Gunsteren, W. F., Billeter, S. R., Eising, A. A., Hünenberger, P. H., Krüger, P., Mark, A. E., Scott, W. R. P. & Tironi, I. G. (1996) *Biomolecular simulation: the GROMOS96 manual and user guide*, BIOMOS & vdf Hochschulverlag AG an der ETH Zurich, Groningen & Zürich.
45. Berendsen, H. J. C., Grigera, J. R. & Straatsma, T. P. (1987) The missing term in effective pair potentials, *J Phys Chem.* **91**, 6269-6271.
46. Humphrey, W., Dalke, A. & Schulten, K. (1996) VMD: Visual molecular dynamics, *J Mol Graph.* **14**, 33-38.
47. Serpell, L. C., Fraser, P. E. & Sunde, M. (1999) X-ray fiber diffraction of amyloid fibrils, *Methods Enzymol.* **309**, 526-36.
48. Sumner Makin, O., Sikorski, P., Serpell, L. C. (2007) CLEARER: a new tool for the analysis of X-ray fibre diffraction patterns and diffraction simulation from atomic structural models, *Journal of Applied Crystallography.* **40**, 966-972.

Table 1. Major fibre diffraction spacings of aligned apoC-II rod-like fibrils formed in the presence of 500 μM LysoMPC.

Meridional spacings (Å)	Equatorial spacings (Å)
4.60 ± 0.01	9.69 ± 0.01
	23.9 ± 0.2
	45.8 ± 0.3

Errors represent the standard error of the mean of four measurements; two independent aligned samples each measured at two distal positions.

Figure legends

Figure 1. The kinetics of apoC-II fibril formation. Fibril formation was initiated using 1 mg/ml WT apoC-II (black circles), D69K apoC-II (blue triangles), K30D apoC-II (red squares) and KDDK apoC-II (green diamonds) in 100 mM sodium phosphate buffer pH 7.4 at 20 °C. Fibril formation was monitored by ThT fluorescence in the absence (A) and presence of 500 µM LysoMPC (B). Data are presented as the mean of two independent measurements. Error bars represent the standard deviation.

Figure 2. Transmission electron microscopy images of apoC-II fibrils. Fibrils were formed by incubation of apoC-II samples (1 mg/ml) in 100 mM sodium phosphate buffer pH 7.4 with 500 µM LysoMPC at 20 °C for 750 h. Samples were diluted to 0.1 mg/ml with distilled water prior to imaging. (A,B) WT apoC-II; (C,D) D69K apoC-II; (E,F) K30D apoC-II; (G,H) KDDK apoC-II. Scale bars are 100 nm.

Figure 3. Cross seeding of apoC-II fibril formation. Fibril formation in 100 mM sodium phosphate buffer pH 7.4 in the presence of 500 µM LysoMPC was monitored by ThT fluorescence at 20 °C. Rod-like fibril seeds, obtained by freeze–thaw treatment, were added at a ratio of 2% w/w to apoC-II solutions (1 mg/ml). (A) WT; (B) D69K; (C) K30D and (D) KDDK apoC-II. Rod-like fibril seeds used were WT seeds (black circles), D69K seeds (blue triangles) and K30D apoC-II seeds (red squares). Control experiments for each variant were carried out in the absence of fibril seeds or LysoMPC and are shown as symbols connected by dashed lines. Data are presented as the mean of two independent measurements. Error bars represent the standard deviation.

Figure 4. Transmission electron microscopy images of seeded fibrils grown in the presence of KDDK apoC-II. Rod-like fibril seeds obtained from freeze-thaw treatment of WT, D69K and K30D rod-like fibrils were added at a ratio of 2% w/w to KDDK apoC-II (1 mg/mL). Samples were incubated in 100 mM sodium phosphate buffer pH 7.4 with 500 µM LysoMPC at 20 °C for 300 h. (A,B), WT seeds; (C,D), D69K seeds and (E,F), K30D apoC-II seeds. Samples were diluted to 0.1 mg/ml with distilled water prior to imaging. Scale bars are 100 nm.

Figure 5. 2D ^{1}H–^{15}N SOFAST HMQC spectra for [^{15}N] apoC-II rod-like amyloid fibrils freshly dissolved and dissociated in 95% d_6-dimethyl sulphoxide (DMSO), 4.5% D_2O, 0.5% d_2-dichloroacetic acid (d_2-DCA). (A) Fully protonated reference sample. (B) [^{15}N] apoC-II fibril sample resuspended in 2.5 mM Tris-HCl buffer, 100% D_2O, pH 7.4 and incubated for 24 h at

20 °C. Residue specific assignments are indicated. (C) Residue-specific protection of rod-like fibrils expressed relative to fully protonated fibrils. Black circles are for prolines residues.

Figure 6. Stern-Volmer plots for acrylamide quenching of the intrinsic tryptophan fluorescence of apoC-II samples. Stern-Volmer plots of freshly prepared apoC-II (black open circles) and apoC-II samples (1 mg/ml) incubated in sodium phosphate refolding buffer, pH 7.4, at 20 ºC for 750 h in the absence (blue closed circles) or presence of 500 μM LysoMPC (red open triangles). The lines drawn through the data are best-fit lines calculated as described previously [12]. Data are presented as the mean of two independent measurements. Error bars represent the standard deviation.

Figure 7. Energy minimised starting structures used for MD simulations. Pre-formed apoC-II (56-76) fibril 12-mers were arranged into three different parallel and anti-parallel arrangements. Straight fibril models for simulation were composed of two apoC-II molecules per rise joined in a cross-β structure with ~4.8 Å distance between the β-strands and ~10-11 Å intersheet separation.

Figure 8. Secondary structure content, β-strand (E, blue) and turn (T, orange), determined from the MD simulations of three different parallel (above) and anti-parallel (below) cross-β arrangements of apoC-II(56-76) 12-mer. The average percentage time each residue spends in the respective conformation at equilibrium, together with the most favourable cluster structure and population are also shown. The secondary structure content was calculated on the middle four strands, shown as opaque color in the image inset.

Figure 9. X-ray diffraction analysis of rod like fibrils. (A) X-ray diffraction pattern from aligned WT rod-like fibrils formed at 1 mg/ml in the presence of 500 mM LysoMPC. The meridional (fibril) axis is horizontal (dashed line) and the equatorial axis is vertical. The lower left quadrant shows a simulated diffraction pattern calculated using the fibril cross section model consisting of two antiparallel copies of parallel arrangement 3 shown in (B). Solid dark grey arrows indicate positions of the two longer equatorial spacings in the simulated diffraction pattern.

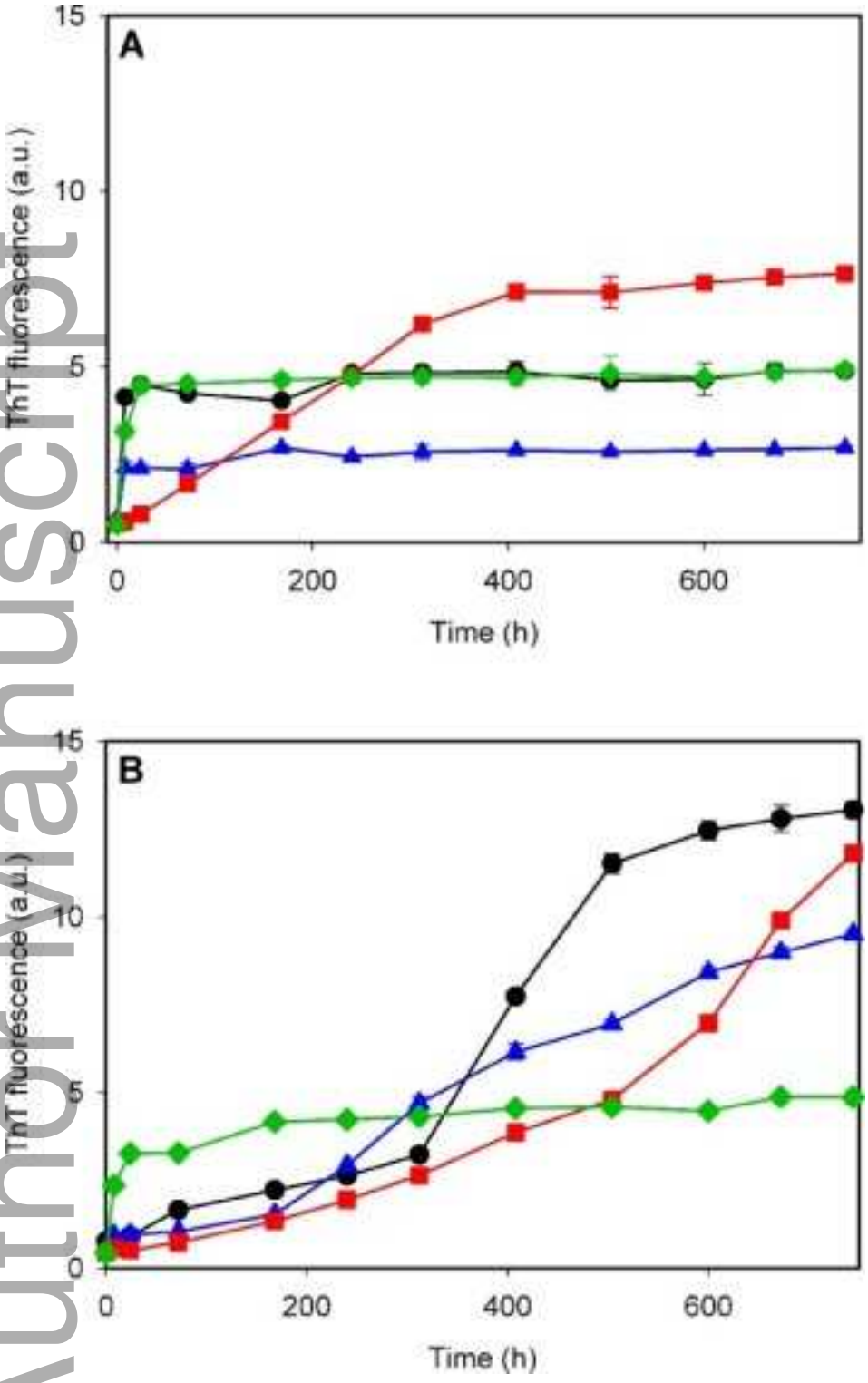

febs_14517_f1.tif

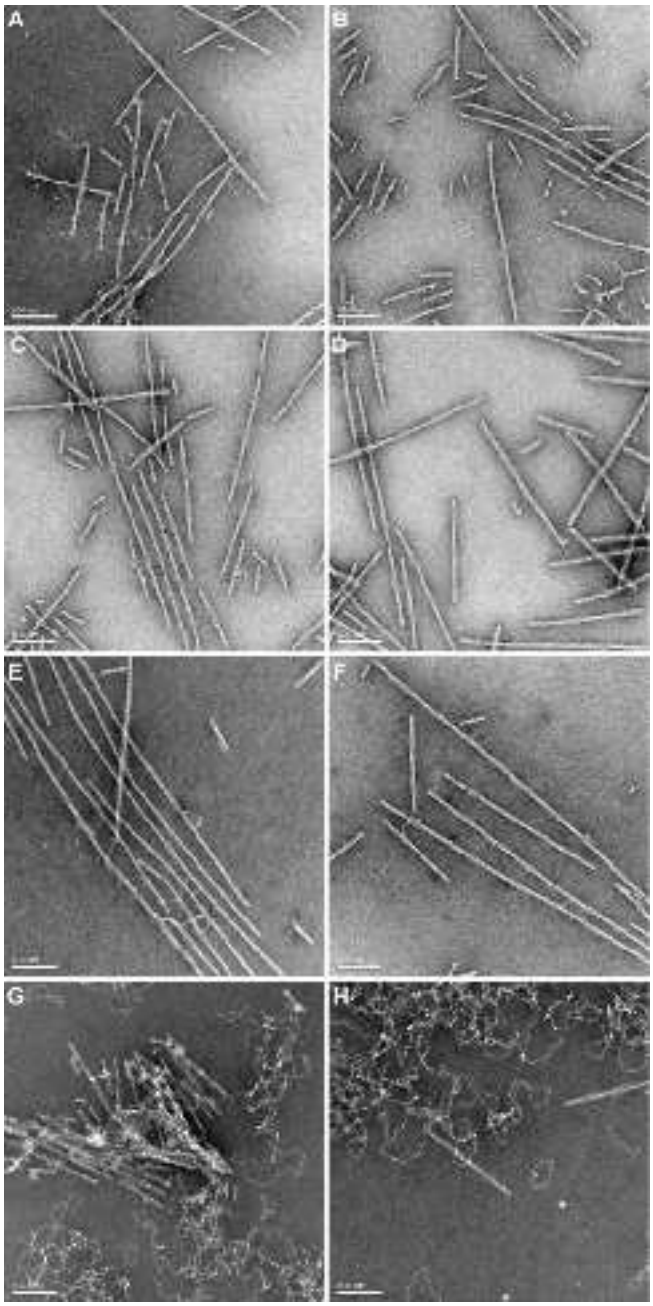

febs_14517_f2.tif

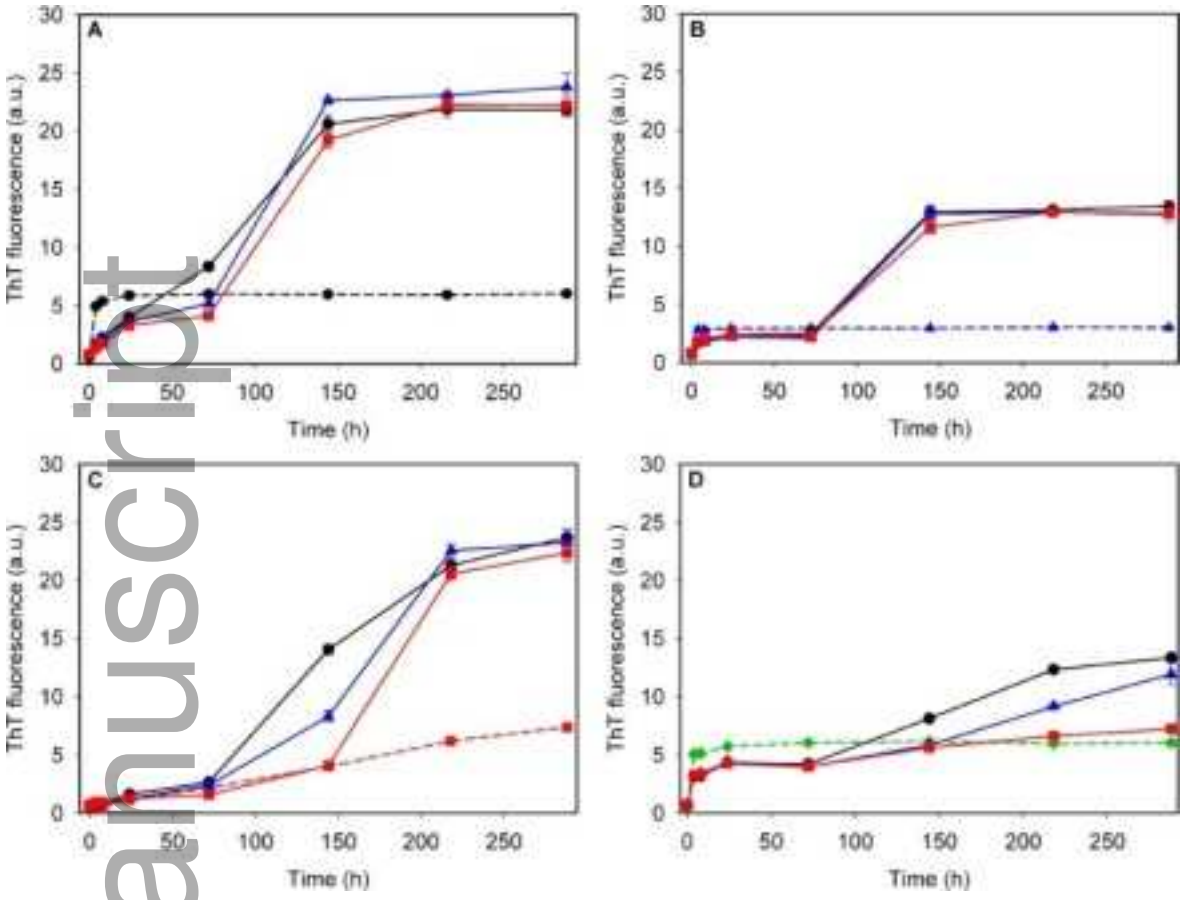

febs_14517_f3.tif

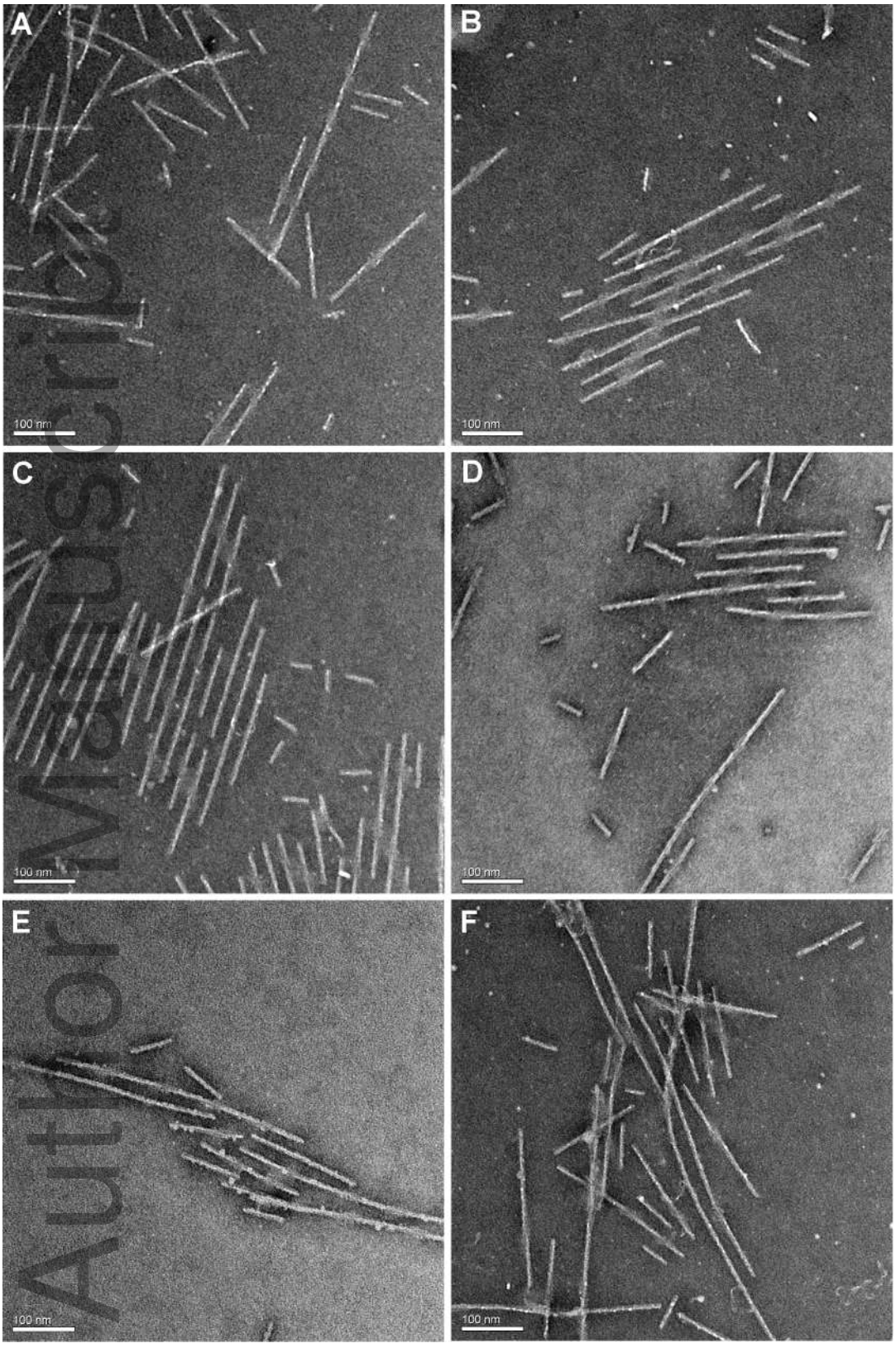

febs_14517_f4.tif

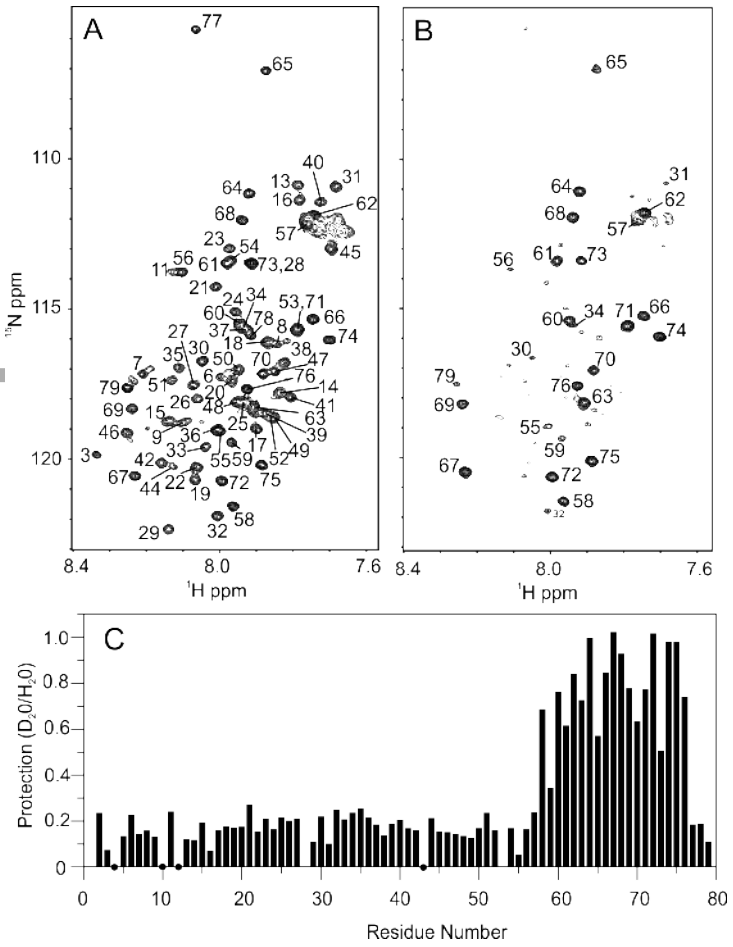

febs_14517_f5.tif

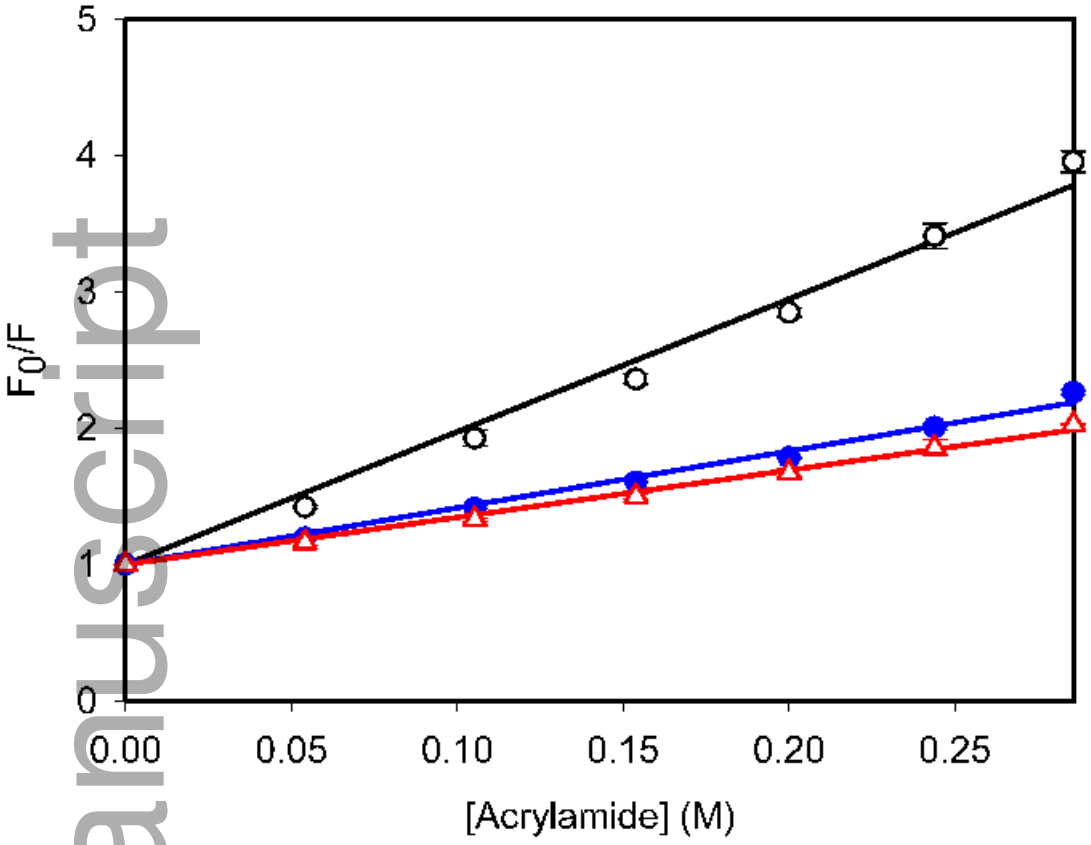

febs_14517_f6.tif

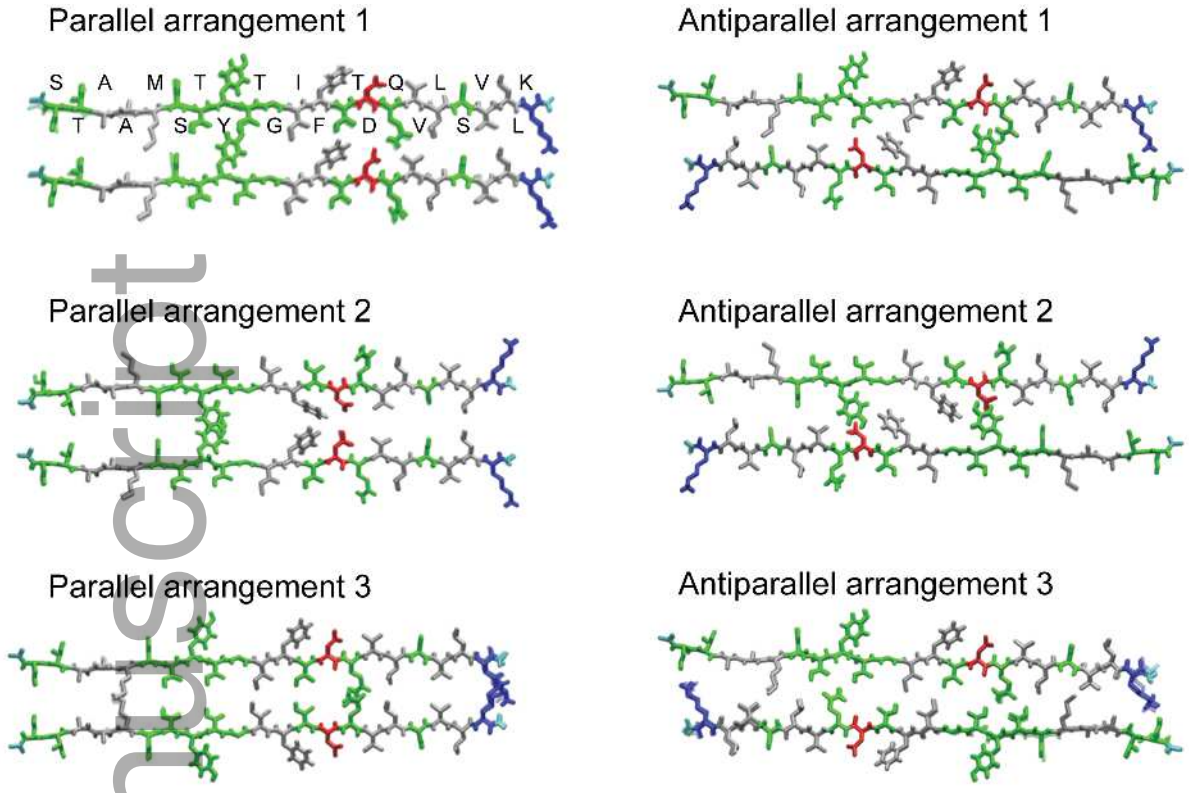

febs_14517_f7.tif

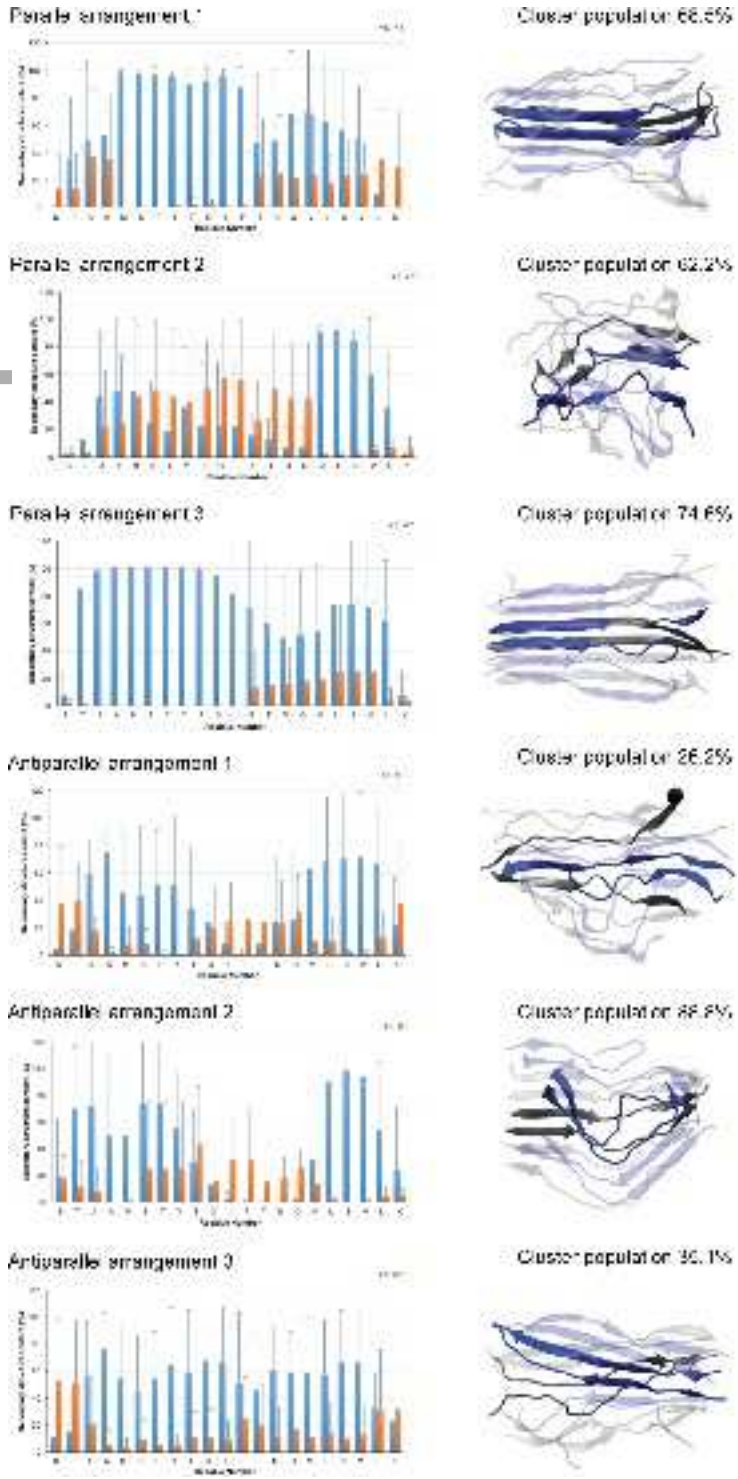

febs_14517_f8.tif

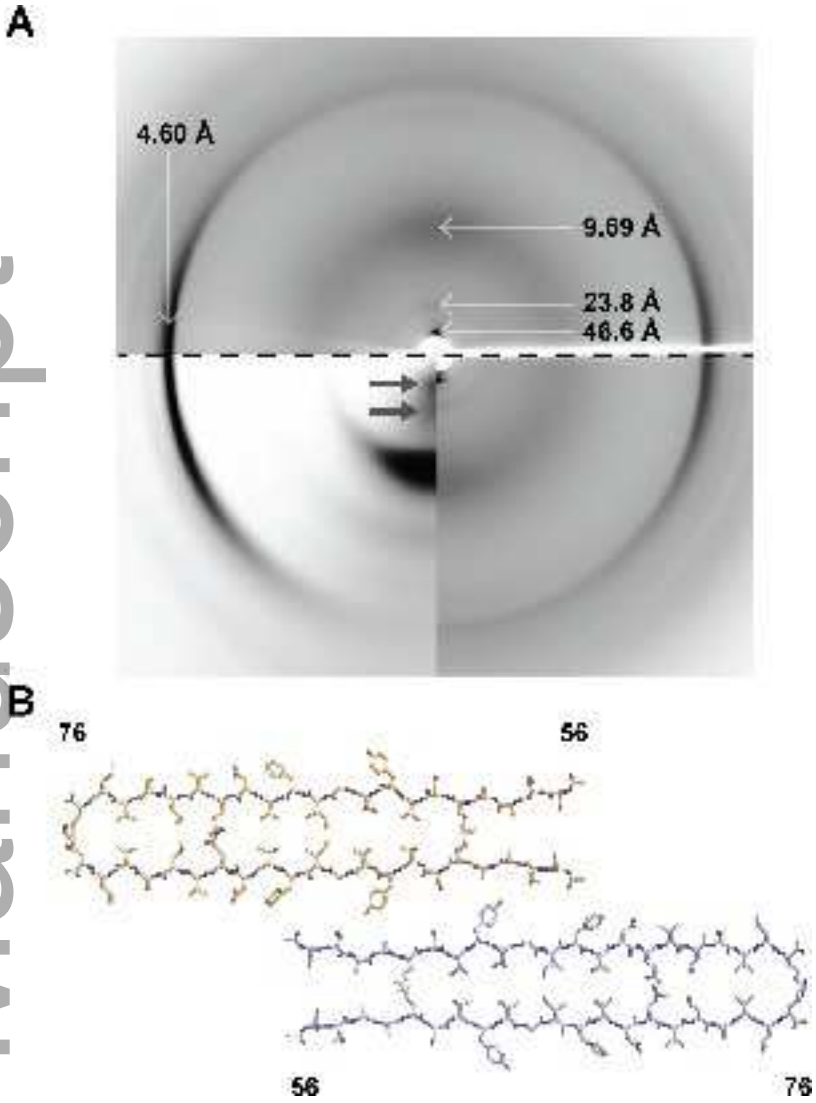

febs_14517_f9.tif